Light weighed: on the statistics and systematics of weak gravitational lensing

Smit, D.M.

3

Weak lensing by very low redshift groups: analysis of systematics and robust shape measurements

Weak gravitational lensing is one of the most direct ways to study mass distributions on a wide range of scales. Here we attempt to complement dynamical and luminosity based mass estimations of nearby light galaxy groups with measurements based on weak gravitational shear.

Shape measurements are derived using two pipelines: the Shapelets technique, describing the intensity distribution of faint background sources in Gauss-Hermite expansions, and the extensively used KSB technique. This allows adequate flexibility in modelling the various distortions that affect the images, such as gravitational shear and systematic effects like the PSF.

We present shear estimates obtained from wide-field imaging data of 79 light galaxy groups from the *Zürich Environmental Survey*. We discuss the level of control of systematic errors and compare results between pipelines. The robustness of the methods is promising. We then derive estimates for the velocity dispersion by fitting the lens profile for a singular isothermal sphere, and discuss estimates for the mass and concentration of the groups, by fitting a Navarro, Frenk & White profile. This provides results to be compared to those of groups at intermediate redshifts, exploring ranges in mass and redshift that have not been studied extensively.

M. Smit, K. Kuijken, T. Schrabback, A. Cibinel, C.M. Carollo, and A. Amara

3.1 Introduction

Weak gravitational lensing, since its first detection by Tyson et al. (1990), has become an important and well tested tool in studying the distribution of mass in the universe. The systematic distortion of background images due to the gravitational bending of light rays by a foreground density field can be described by a straightforward geometric model (see e.g. Hoekstra 2005, for a review), instead of relying on complicated physical models of luminous matter or sometimes sparse dynamical tracers.

In the past decade a standard cosmological model has crystallised out of a wide range of measurements of increasing precision. In this model, the matter content of the universe is dominated by a dark, gravitationally interacting component which is thought to form the background density structure for the formation of galaxies and galaxy concentrations as fundamental cosmological building blocks. One of the key aspects in understanding galaxy and structure formation is therefore testing the relation between the visible over-densities and the associated dark matter halos.

On larger scales, up to those of clusters and superclusters, and on small scales, the lensing by individual galaxies first detected by Brainerd et al. (1996), successful estimates of the dark matter content have been made during the last decade (see e.g. Hoekstra et al. 2004, Mandelbaum et al. 2006, Heymans et al. 2006). On intermediate scales however, when trying to detect the common halos of (light) galaxy groups, progress has been slower (see e.g. Mandelbaum et al. (2006) and Leauthaud et al. (2010) for results in the high mass group regime). An important reason for this is the lack of systematic surveys of galaxy groups in combination with robust, extensive catalogues of galaxy groups.

Hoekstra et al. (2001) reported the first measurements of the average mass and mass-to-light ratio (M/L) of light galaxy groups (~ 4 members) around a median redshift of $z = 0.33$, using groups in the CNOC2. This sample was extended in Parker et al. (2005), who found an average velocity dispersion of $\sigma \simeq 245 \pm 18$ km s^{-1} and $M/L_B \simeq 185 \pm 28\ h\ M_\odot/L_{B\odot}$.

As most galaxies are probably found in groups (see e.g. Eke et al. 2004), it is a necessity to understand the group environment and its effect on galaxy evolution. There are indications that a significant part of galaxy evolution already takes place in these environments, before being assembled in clusters (see e.g. Tran et al. 2009). Lensing might prove to be an important independent tool, when studying light, unrelaxed structures with low numbers members.

In recent years, well-defined group catalogues have become available from large surveys like the Sloan Digital Sky Survey (SDSS, Abazajian et al. 2003) and the 2-degree Field Galaxy Redshift Survey (2dFGRS, Colless et al. 2001), that allow systematic studies of galaxy concentrations. Weak lensing may provide a crucial, independent complement to dynamical and luminosity-based mass estimations for these systems that are sometimes sparsely populated and in often unknown phases of evolution. This research, using groups from the *Zürich ENvironmental Survey* (ZENS, Carollo et al. 2013), may be a suitable pathfinder for the Kilo-Degree Survey (KiDS), which is scheduled for 2009 and has an extensive overlap with the 2dFGRS and this sample.

Weak lensing itself has its own limitations, due to intrinsic variations in the shapes of distant sources (a statistical limitation called shape noise) and the ever present systematic errors (most notably the distortions induced by the PSF). In the last decade, several methods for shape measurements have been proposed and used (see e.g. Kaiser et al. (1995) [*KSB*], Hoekstra et al. (1998) and Erben et al. (2001) [*KSB+*], Bernstein & Jarvis (2002) [*BJ02*], Re-

fregier (2003) and Kuijken (2006, hereafter KK06) [*Shapelets*], Miller et al. (2007) [*Lens*fit], among others). In order to make a sensible analysis of the expected weak signal of these light systems, a thorough understanding of these systematics and an adequate method for correcting for these is required.

This paper is ordered as follows. In the next section, we briefly describe the data set. The third section outlines the methods of shape measurement while the fourth presents the actual measurements, the systematic distortions present in the data, and the robustness of our shear estimates. In section 5 we present the signal obtained from these measurements and we discuss several fits to the shear profiles. The final section contains the conclusions.

Unless specifically mentioned otherwise, we assume a ΛCDM cosmology with $\Omega_m = 0.3$, $\Lambda = 0.7$ and $H_0 = 70h$ km s^{-1} Mpc^{-1}. Throughout the paper we discuss various selection criteria for stars and background sources to be used in the final quantitative analysis. Unless mentioned otherwise to highlight or discuss the effect of a certain criterion, figures of source distributions or source comparisons will show the same *final* selection, to make comparing figures throughout the paper intuitively clear, even where the final selection is not yet completely discussed. Finally, we discuss the determination of the group centres. In figures and discussions where group (centre) positions are mentioned, we assume the luminosity weighted mean (LWM) position of the group members as explained in Section 5, except where indicated otherwise.

3.2 Data

For this analysis we use Wide Field Imager (WFI) observations of 79 nearby galaxy groups from ZENS, ESO Large Programme 177.A-0680 (Carollo et al. 2013). ZENS is based on a sample of 1630 galaxies, members of 141 galaxy groups extracted from the 2dFGRS (Colless et al. 2001), and specifically from the Percolation-Inferred Galaxy Group (2PIGG) catalogue (Eke et al. 2004). The 141 ZENS groups are a random selection of the complete 2PIGG sample of 185 which are found in the very thin redshift slice $0.05 < z < 0.0585$, and have at least 5 confirmed members in the 2PIGG catalogue, down to a magnitude $b_J = 19.45$. The ZENS sample is thus statistically complete, and free from possible biases deriving from distance effects. It covers two orders of magnitude in dynamical mass scales, ranging from poor ($\sim 10^{12} M_\odot$), to rich galaxy groups.

This paper is based on the optical B and I images for the first set of 79 groups out of the total sample of 141, that were acquired during several observing runs in January-February 2005 and April 2006-March 2007 with the WFI camera mounted at the Cassegrain focus of MPG/ESO 2.2m Telescope at La Silla. Each group was observed in 5 dithered exposures in the B- and I-band, with single exposure times between 131 and 144 seconds. In each band, the final science image was obtained by taking the median of the five dithered exposures, so as to remove cosmic ray and CCD defects (see Carollo et al. 2013, for a detailed discussion of the data reduction).

The 79 groups have a median velocity dispersion of $\sigma \sim 210$ km sec^{-1} ($38 \leq \sigma \leq 691$ km sec^{-1}) and a median total luminosity of $L \sim 5.0 \times 10^{10} L_\odot$ ($1.1 \times 10^{10} \leq L \leq 5.9 \times 10^{11} L_\odot$). The median number of catalogued group members is 8, with the number of members ranging from 5 to 71.

The observations cover a total area of the sky of ∼22 deg^2 to a depth of $I_{AB} \sim 22$ at S/N

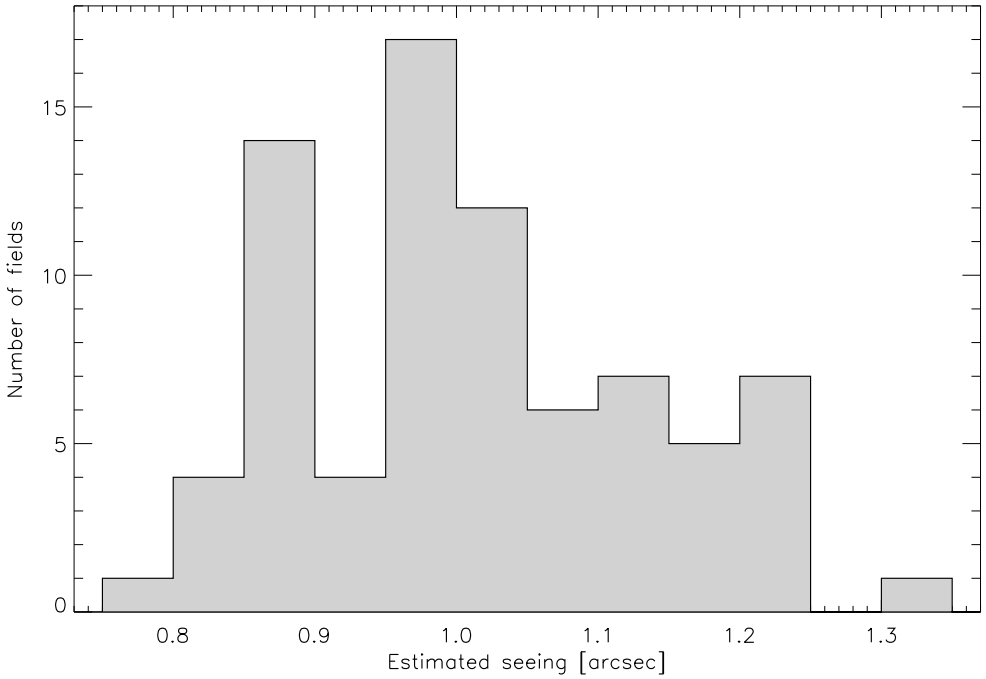

Figure 3.1: Histogram of the seeing of individual fields, as determined from the location of the stellar locus.

~ 10 for extended background sources which we use for our analysis, for a total of more than 10^5 sources ($\sim$ 2000 per field, ~ 2 arcmin^{-2}). The selected fields have a median seeing in the I-band of $\sim 1.0''$ arcsec (Figure 3.1), ranging between $0.75''$ and $1.35''$.

Figure 3.2 shows the magnitude distribution of detected sources that pass the selection criteria that will be discuss in the following sections, i.e. the sources shown are the sources used in the final scientific analysis, but including sources of magnitudes brighter than the $I_{AB} \geq 19$ magnitude criterion used. The magnitude distribution is shown as

$$n_{\rm eff}(I) = \frac{N_{\rm eff}(\Delta I)}{N_{\rm eff,tot}} \tag{3.1}$$

where $N_{\rm eff,tot}$ is the *effective* total source count, including individual weights discussed in Section 3, so the sum of the histogram equals 1.

3.3 Methods

Weak lensing by a foreground density distribution introduces a systematic alignment of background sources. Hence, the (reduced) gravitational shear can be estimated from the shapes of these sources. Any systematic effect that distorts these shapes and can mimic the gravitational lensing signal or affect our shape measurements, such as atmosphere, camera distortion, and pixelisation, needs to be identified and corrected for.

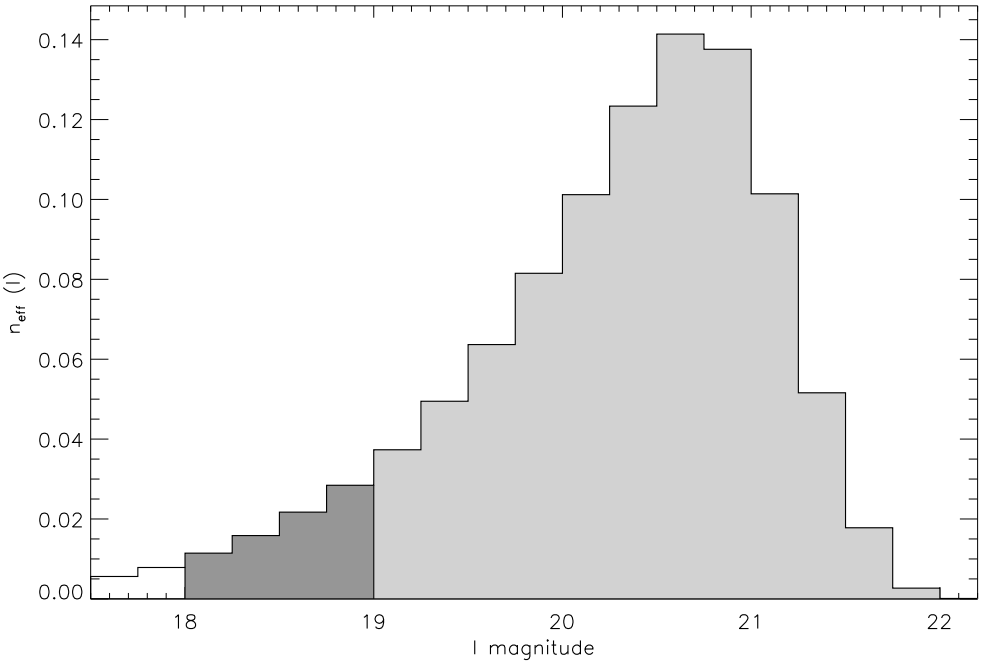

Figure 3.2: Magnitude distribution of the background source sample, determined by the selection criteria discussed in this paper, but including sources of all magnitudes, represented as part of the effective total source selection, so the sum of the histogram equals 1. The light grey area represents the sources used for the final quantitative analysis. The dark grey area represents sources with $18 \leq I \leq 19$, which are not used in the final analysis.

In this section we briefly discuss gravitational lensing and the Shapelets method introduced in KK06. The KSB method and various modifications have been extensively used and were discussed in the aforementioned papers. Therefore, we only briefly touch upon the implementation we use. Both methods have been tested in the Shear TEsting Programme (Heymans et al. 2006, Massey et al. 2007, hereafter STEP) and for a thorough discussion of the results, we refer the reader to these papers.

3.3.1 Weak gravitational lensing terminology

The light rays emanating from different parts of an extended source in the background of a gravitational lens will experience different parts of the (projected) lens potential and will therefore be deflected slightly differently. The resulting change of the source shape, essentially a coordinate transformation $I(x, y) \rightarrow I(x', y')$ is described in terms of the convergence κ and the shear: (γ_1, γ_2)

$$\begin{pmatrix} x' \\ y' \end{pmatrix} = \begin{pmatrix} 1-\kappa-\gamma_1 & -\gamma_2 \\ -\gamma_2 & 1-\kappa+\gamma_1 \end{pmatrix} \begin{pmatrix} x \\ y \end{pmatrix} \tag{3.2}$$

Since we don't know the intrinsic source sizes or magnitudes, we can only measure the net *distortion* or *reduced shear* $(g_1, g_2) \equiv (\gamma_1, \gamma_2)/(1-\kappa)$:

$$\begin{pmatrix} x' \\ y' \end{pmatrix} = (1-\kappa) \begin{pmatrix} 1-g_1 & -g_2 \\ -g_2 & 1+g_1 \end{pmatrix} \begin{pmatrix} x \\ y \end{pmatrix} \tag{3.3}$$

where the transformation is written as a multiplication $(1-\kappa)$, which we don't identify, and a distortion matrix describing the alignment of lensed sources.

The *tangential* shear g_+, often termed the E-mode, is defined as the reduced shear g_1 in the coordinate system with the lens at the origin and the x-axis tangential to the line connecting the observed angular positions of the lens and the source. The g_2 component in the same reference frame is defined as the cross shear $g_\times$ or B-mode.

Following KK06, we define the ellipticity (e_1, e_2) of an object such that a distortion $(-e_1, -e_2)$ will circularise the best-fitting model with constant-ellipticity isophotes. This way, a gravitationally lensed, intrinsically elliptical source can be described as a circular source being sheared twice: first by (e_1, e_2) and then by (g_1, g_2) (see also BJ02).

Background sources display an intrinsic variation in ellipticity and orientation, which is a form of random (shape) noise in estimating the reduced shear. For a source sample with shape noise that is indeed random, we expect $\langle e_i \rangle = 0$, allowing us to recover an estimate for $\langle g_i \rangle$ using a sufficiently large source sample.

3.3.2 Shapelets

In the Shapelets formalism introduced by Refregier (2003), the light distribution of a source is expanded in the orthonormal basis set of Gauss-Hermite functions. This allows for a flexible model and has the advantage that the behaviour of these basis functions under simple transformations (such as an applied shear or smearing by a PSF) is well understood. A PSF model can then be constructed from the shapelet expansions of bright stars in the image, for which the expansions of sources can be corrected in a consistent manner.

In this analysis we use the KK06 implementation of Shapelets (the KK pipeline in STEP), which describes sources as sheared circular objects. As mentioned above, the measured ellipticities are then geometric: a superposition of the intrinsic shape, expressed as a shear, and the gravitational shear. To correct for PSF effects, this sheared circular galaxy model is convolved with the constructed PSF model and fitted to the observed sources.

$$M = P \cdot (1 + g_1 S_1 + g_2 S_2 + \delta_1 T_1 + \delta_2 T_2)(c_0 C^0 + c_2 C^2 + \ldots) \tag{3.4}$$

Here M is the fitted model, the C^n are the basis functions describing a circular source, c_n are the coefficients to be fitted, S_i and T_i are the first order complex shear and translation operators respectively, γ_i and δ_i are the fitted shear and translation (to ensure an optimal centroid fitting) and P is the PSF convolution matrix. Not only is this numerically more stable than a deconvolution of the sources, it also allows for error propagation of the pixel noise.

The sources and stars are all expanded to a fixed order of $n = 12$ in basis functions, to avoid truncation biases in the shape measurements. The images contain enough stars to ensure a well-sampled PSF, $N_* \approx 900$ ($n_* \approx 1$ arcmin^{-2}), and we model the PSF variation of the field by a polynomial of order 5.

Based on the pixel noise, we define individual weights for the sources as

$$w = \left(\sigma_{sn}^2 + \sigma_{g_1}^2 + \sigma_{g_2}^2\right)^{-1} \tag{3.5}$$

where σ_{sn} is the intrinsic shape noise, to avoid spuriously large weights, and σ_{g_i} are the estimated uncertainties in the ellipticity components.

In addition to other selection criteria described in section 4, we select sources with a minimum size compared to the smearing induced by the PSF. We exclude sources for which $\beta_i > 1.1\beta_*$, where β is the scale radius of the Gaussian basis of the shapelet expansion, with subscripts indicating the original source before convolution with the PSF and the stars, respectively.

3.3.3 KSB+

KSB uses the first order effects of distortions induced by gravitational shear and PSF on the weighted second moments of the light distribution of a source to estimate the reduced shear. We have obtained an independent shape measurement catalogue using KSB+ based on the implementation by Erben et al. 2001, with modifications by T.S. (the TS pipeline in STEP).

We define individual weights for this method analogous to those for the KK pipeline, based on the variance of the shear estimators from this pipeline. Based on the findings in the STEP analyses, we expect an underestimation of the shears by KSB of $\sim 8\%$. We have applied a 'fudge-factor' to account for this expected bias, based *only* on the results from simulations.

In addition to other selection criteria described in the following section, we filter for KSB shape measured S/N ≥ 4, to be consistent with KSB+ studies using a similar definition of the source S/N. In this pipeline, the effect of smearing and shearing by the PSF is for an important part described by the P^g tensor. To avoid being dominated by noise, we exclude sources for which $\mathrm{Tr}(P^g)/2 < 0.1$ and the half light radius of the source compared to that of the average star is not at least $r_h > 1.2r_h^*$ (see Erben et al. 2001, for technical details and terminology).

3.4 Shape Measurements

We explain and justify an a priori selection and exclusion scheme, completely 'blind' to the final scientific result.

For our analysis we use as mentioned earlier only sources which are detected at a minimum S/N of ~ 10 in flux. Any sources which suffer from very close neighbours, truncation effects due to chips edges or other uncertainties in their photometry are flagged and excluded. Any remaining neighbour that is extended enough to affect the intensity distribution of the source will induce power in high order coefficients. Since these should be close to zero in our shapelet expansions, we flag and exclude these sources as well.

We estimate a shape noise of $\sigma_{sn} \simeq 0.25$ in the KK measurements, and $\sigma_{sn} \simeq 0.28$ in the TS measurements. The presence of noise in any real data incurs a small fraction of unrealistically large ellipticities, expressed as a shear greater than unity. We exclude any sources with estimated errors $\sigma_g > 0.4$. In the case where we calculate statistical averages, sensitive to outliers, we also exclude total ellipticities $|g| > 2$, which is not too strict in order to avoid inducing a bias in the observed distribution in ellipticities.

At the edges of the field of view, systematic distortions are often most severe, but close to edges of the detector there are not always enough stars to optimally model this. In our selection, we exclude sources from the corners of our images.

For bright sources, the stellar locus is well separated from the galaxy distribution. For faint sources, contamination of one by another is almost a certainty. We only use unsaturated stars with $I_{AB} \leq 22$ for PSF modelling. As mentioned in the previous section, we exclude galaxies smaller or comparable to the widest stellar images from our selection, on a field by field basis to account for variations in the seeing.

In the rest of this section, we discuss the robustness of our shape measurements and the sensitivity to residual systematic effects. We estimate the redshift distribution of the sources and possible contamination by faint foreground sources. This leads to the final selection criteria for background sources to be used in the gravitational lensing analysis of section 5.

3.4.1 Robustness

To investigate the robustness of our shape measurement methods, we have made several consistency checks and compared the results.

Comparing methods

In the left panel of Figure 3.3, we compare the shear estimates derived by the KK and the TS pipelines. Taking into account the uncertainties in both sets of measurements, we fit a linear relation

$$g_{i,TS} = (1 + m)g_{i,KK} + c \tag{3.6}$$

where m represents a multiplicative bias and c an additive bias. Comparing $\sim 1.5 \times 10^5$ sources, we find an excellent agreement between the pipelines on this data set, with very tight constraints on the biases, giving $m \simeq 0.1 \pm 0.1$ % and $c = 0.0 \pm 0.1$ %. Only for the noisiest outermost contour, a slight bias at very high ellipticities can be argued for.

Although no bias means that the measurements are *on average* the same over the whole selection, the variance perpendicular to the best fit line gives an indication of the tightness of the correlation, or the variation between individual measurements. We measure a standard deviation around the best fit line of $\Delta g \simeq 5.6$ %, which can be seen as a small, negligible contribution of random noise compared to the estimated shape noise of our source selection.

This result is a confirmation of the robustness of our shape measurement techniques and for this data set, we can conclude that the two pipelines essentially give the same measurements. The estimated uncertainties and the associated weights do vary between the methods.

Stacked images and single exposures

Using the same initial detection catalogues derived from the stacked science images, we have run the Shapelets pipeline on individual exposures for a single field. These single frames are noisier by a factor of $\sqrt{5}$ and the contribution of the PSF anisotropy pattern to the reduced shear can change significantly from exposure to exposure (see Figure 3.4). These single exposures may contain more defects that are removed in the final dithered stacking, which is why the stacked images were used for detection.

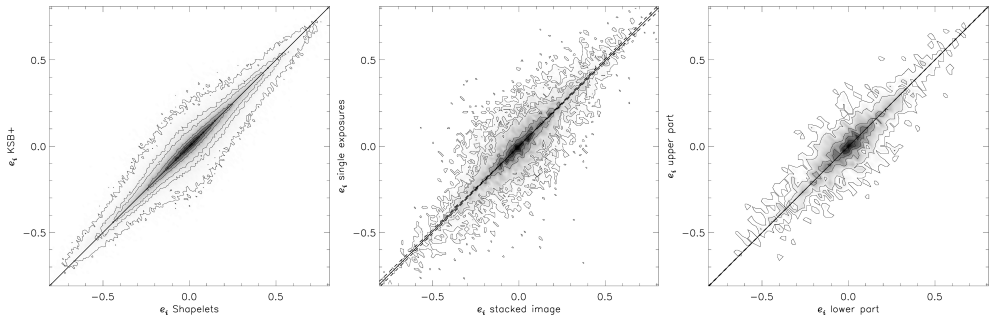

Figure 3.3: *Left:* Shear estimates obtained using the KK Shapelets pipeline compared to shear estimates using the TS KSB+ pipeline. Only at the outermost contour, high ellipticities might start to show a very slight bias. *Middle:* Shear estimates obtained from single exposures of a single field compared to shear estimates obtained from the final stacked image. *Right:* Ellipticities as measured in the "lower" area of the field of view compared to ellipticities of the same sources as measured in the "upper" area of an overlapping field of view. From left to right, the contours exhibit more noise due to statistical power. The spread around the best fit line is comparable. In each figure, the greyscale represents the number count of sources as a 2D histogram. The solid contours, where plotted, correspond to 90%, 70%, 50%, 30%, 10%, 7%, and 4% in counted sources. The solid lines represent the best fit line $e_y = (1 + m)e_x + c$ and the dashed lines represent a 1σ deviation in m. For the left panel $m = 0.1 \pm 0.1$ % and $c = 0.0 \pm 0.1$ %. For the middle panel, $m = -1.1 \pm 2.2$ % and $c = 0.0 \pm 2.2$ % . For the right panel, $m = 0.2 \pm 0.3$ % and $c = 0.1 \pm 0.3$ % .

One of the key questions in the development of accurate shape measurement techniques is the effect of stacking exposures with different PSF on the shapes of the measured sources. Since we have argued earlier that the Shapelets formalism is in principle a method with good flexibility to fit a variety of shapes, we investigate here the performance on the individual PSF patterns for a field where there is significant variation, and the resulting stacked PSF.

In the second panel of Figure 3.3, we compare our shape measurements to ellipticities derived from single exposures, logically only selecting source coordinates actually present in all these exposures. This means we select only stars and background sources from areas on the stacked images that are covered by each of the five exposures, resulting in chip-like regions, as shown in Figure 3.5.

The resulting ellipticities seem slightly noisier than those of the stacked frame, but taking into account the slightly larger measurement error estimates, we find no significant bias between the measurements. The best linear fit gives $m \simeq -1.1 \pm 2.2$ % and $c = 0.0 \pm 2.2$ %.

As we have only $\sim$ 6000 sources in this particular field, we lack the statistics from the comparison between the KK and TS pipelines, which results in *visually* noisier contours. The deviation from the best fitted line is comparable: we measure a standard deviation of $\Delta g \simeq 12$ %, roughly the expected factor $\sim \sqrt{6}$ higher compared to the spread around the best fitted line in the left panel of Figure 3.3.

Another important observation is the lack of bias in the fit between ellipticities. This means that, although the uncertainty estimates are sensitive to the level to which sources extend above the noise, when taking the proper weight factors into account both approaches give the same result, adding to the robustness of the shape measurements.

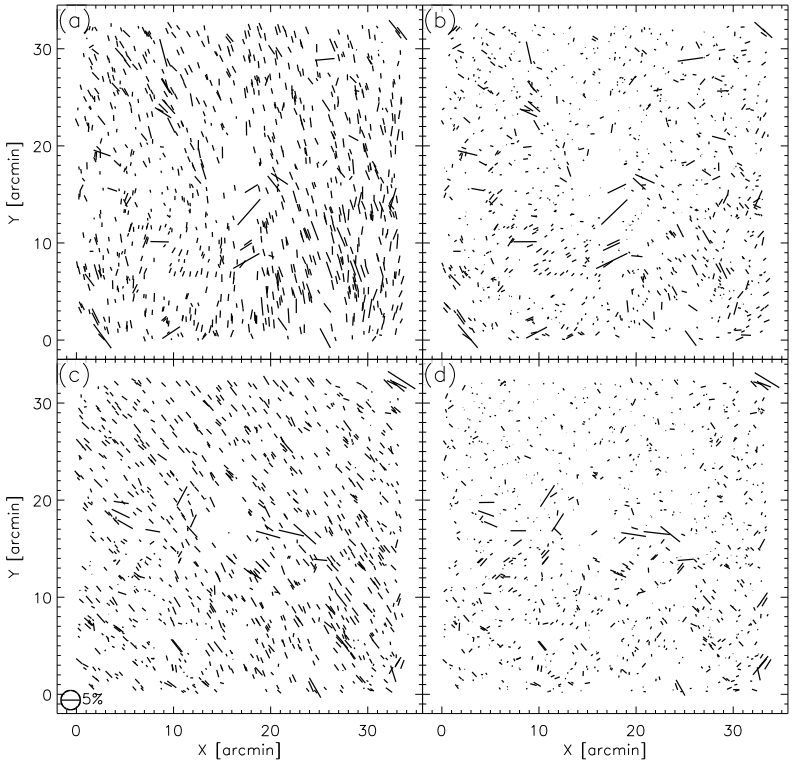

Figure 3.4: Variation of the PSF and PSF correction over exposures of one field. Panels (a) and (b) shows the PSF modelling of an exposure where the pattern displays an almost pure negative g_1 quantitatively; visually, the stars seem to be aligned vertically. In the exposure shown in panels (c) and (d), the PSF introduces an almost pure negative g_2: the pattern of the PSF seems predominantly diagonal.

Overlapping fields

A few of the groups lie close enough to another group from this sample, that observation overlap slightly. This gives us the opportunity to compare measurements of the same sources at different locations in the field of view. In the third panel of Figure 3.3, we compare ~ 600 sources that are detected in two fields.

The choice in which measurement to use as 'reference' value and which as 'comparison' value is completely free. In these data, the x and y image coordinates are almost perfectly aligned with right ascension and declination respectively. In Figure 3.3 we compare the measurements of the northernmost of the two fields, in which the sources lie predominantly in the lower part of the field (i.e. have a lower y image coordinates), to the measurements in the southernmost of the two fields, in which the same sources are detected higher in the field.

We have also made the same comparison selecting on the image x coordinate and we have even made the comparison using random selections. The results in all cases are identical within significance. It is less instructive to fit a linear relationship in this case, but for completeness we note here that we find $m = 0.2 \pm 0.3$ % and $c = 0.1 \pm 0.3$ %. A more

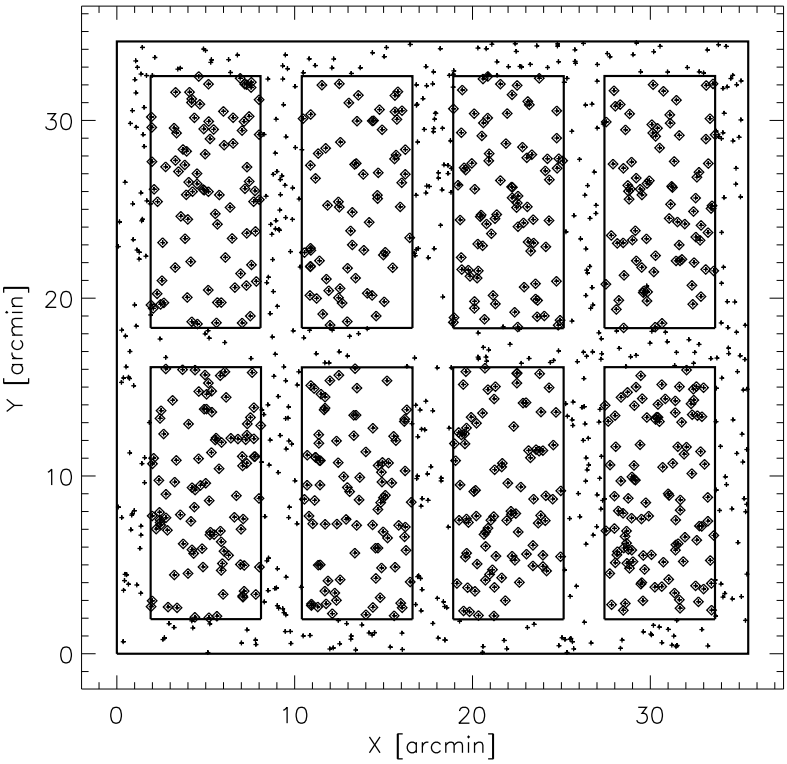

Figure 3.5: The areas on the stacked image that are covered by all five individual exposures. As an example, we show the positions of the stars over the field. Diamonds represent stars in areas with a full depth of exposures.

important result is that the variation around the best fit line is, within significance, the same as for the comparison between the KK and the TS pipelines. We find a standard deviation of $\Delta g \simeq 5.0$ %.

3.4.2 Possible systematics

Given the consistency of our shape measurements between independent methods and observations, we expect any remaining systematic signal to be carried in the actual shapes of background sources and not to be introduced by the measurement thereof.

Since this survey specifically targets groups of galaxies, a concern with this dataset is that we are not dealing with random fields. Although there are a few exceptions, in most of the fields we expect an overdensity concentrated near the center of the field of view. Several diagnostics that are devised for random fields, such as the estimation of a remaining correlation between the PSF and the corrected source shapes, become difficult and less meaningful to interpret.

Near the edges and corners of any field of view, fitted models such as those for the PSF variation or astrometric corrections are expected to become less constrained. For a sample of

lenses predominantly located near the center of the field of view, possible systematics induced by these effects occur at roughly the same distance from each lens and will most likely not disappear by averaging over the lenses.

Astrometric effects

Roughly 30% of the fields have sufficient overlap with SDSS to estimate the possible presence of astrometric distortions. Using the SDSS positions as a reference, we determine the displacement of sources in our catalogues and investigate whether the displacements are random or display a pattern dependent on position on the field. The median displacement is ~ 1.8 pixels or $\sim 0.4''$.

Intuitively, one can understand the effect of astrometry as a distortion as follows. If the field is slightly stretched in the x direction (or compressed in the y direction), this would induce a small, positive e_1: on average, all sources would display a slight horizontal alignment. Similarly if the field is stretched in the y direction (compressed in the x direction), the effect would be a small, negative e_1.

Following the same reasoning for the diagonal directions for e_2, it is clear that we can detect a possible effect by measuring the variation of the displament $(\Delta x, \Delta y)$ of our detection with respect to SDSS as a function of position:

$$\frac{\partial(\Delta x)}{\partial x} - \frac{\partial(\Delta y)}{\partial y} \qquad \text{and} \qquad \frac{\partial(\Delta y)}{\partial x} + \frac{\partial(\Delta x)}{\partial y} \tag{3.7}$$

for e_1 and e_2 respectively.

Translating this into $(e_+, e_\times)$ with respect to the groups, we do not detect a significant deviation from zero at any distance from the expected lens positions, with maximum error bars of the order of 10^{-4}.

PSF discontinuities

As already mentioned, a dominant source of systematic distortion of source shapes is the PSF. Using the shapelet expansions of the stars, we investigate in Figure 3.6 how much spurious signal can be expected to be contaminating the true lensing signal. The differences between the shapes of the stars and the PSF model fitted to those stars should be consistent with zero for any observation. This provides a diagnostic for residual PSF distortions present in the data that should not be affected by image geometry or lens positions in the fields of view, as long as the distribution of foreground stars is sufficiently random.

Plotted are both the tangential and cross distortion deduced from the stellar shapes, mimicing a $(g_+, g_\times)$ induced by the original PSF, and the residual effect carried in the stars after correction. The average PSF pattern exhibits only a small cross signal which largely disappears after correction. The tangential pattern shows more variation, however. While the *average* residual distortion after correction for the PSF vanishes by construction, there remains a subpercent but significant postive signal close to the group centers and a similar but negative signal on large scales.

To investigate the cause of this residual signal, we have looked at the spatial variation of the stellar residuals over all fields. In Figure 3.7 we show one of the results of these tests, the variation of residual ellipticity of foreground stars over the field. We have used all $\sim 6 \times 10^4$ stars of all fields and their positions with respect to the central pixel of each image.

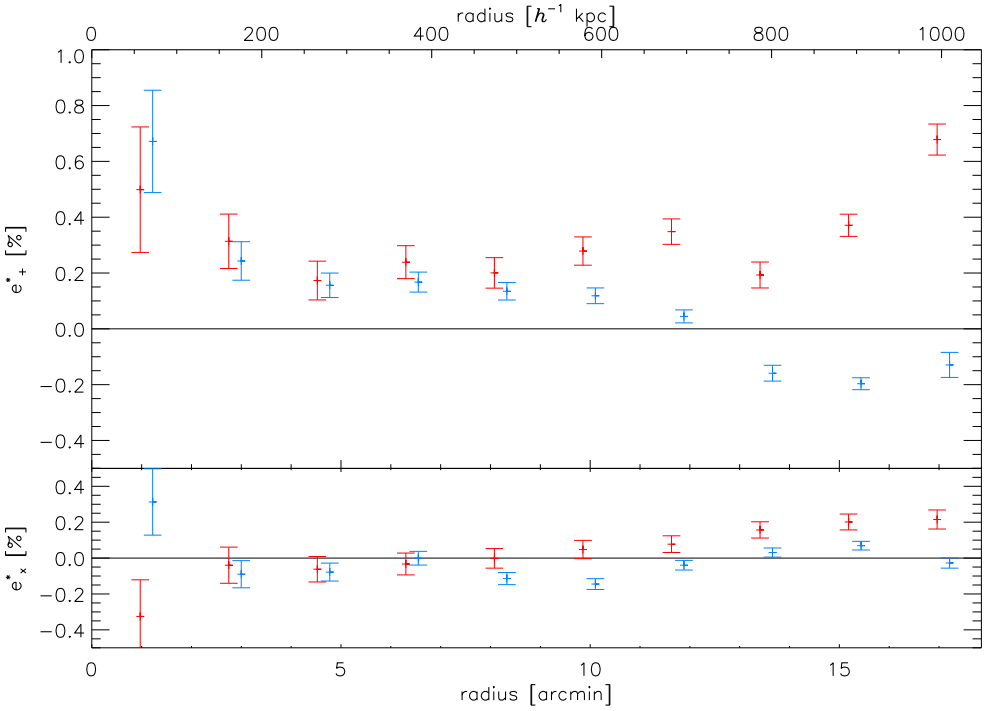

Figure 3.6: Tangential ellipticity (e_+) and cross signal ($e_\times$) with respect to the ZENS group centres, carried in the stars before (red) and after (blue, slightly offset to the right) correction for the PSF. The total number of stars used is $\sim 6 \times 10^4$.

The layout of the WFI chips stands out clearly, showing higher residuals in regions that lie between chips in one or more exposures. This is to be expected, as the PSF model is dominated by the chip-like regions covered by all individual exposures. This model is less representative in the regions where one of more exposures don't contribute to the PSF, resulting in a less accurate PSF correction in these regions.

To test the effect of these PSF residuals in the stars, we plot in Figure 3.8 the same tangential and cross distortions as in Figure 3.6, but using only stars that are covered by all individual exposures. The result is a significant improvement in the residual tangential PSF distortion. Except for two of the outer bins, the signal carried by the stars disappears after PSF correction, showing that the PSF model is much more accurate in these regions. The residual cross signal is also dimished further, being consistent with zero on all scales.

For our PSF model and correction and for the analysis and interpretation in Section 5, we will only select stars and background sources that are covered by all individual exposures. This selection reduces the number of stars and background sources by approximately 35%, to $N_* \approx 3.5 \times 10^4$ and $N_s \approx 10^5$. A more efficient approach would be to account for the PSF of each individual exposure and combine the information, similar to the *lens*fit pipeline (Miller et al. 2007), but this is beyond the scope of this project.

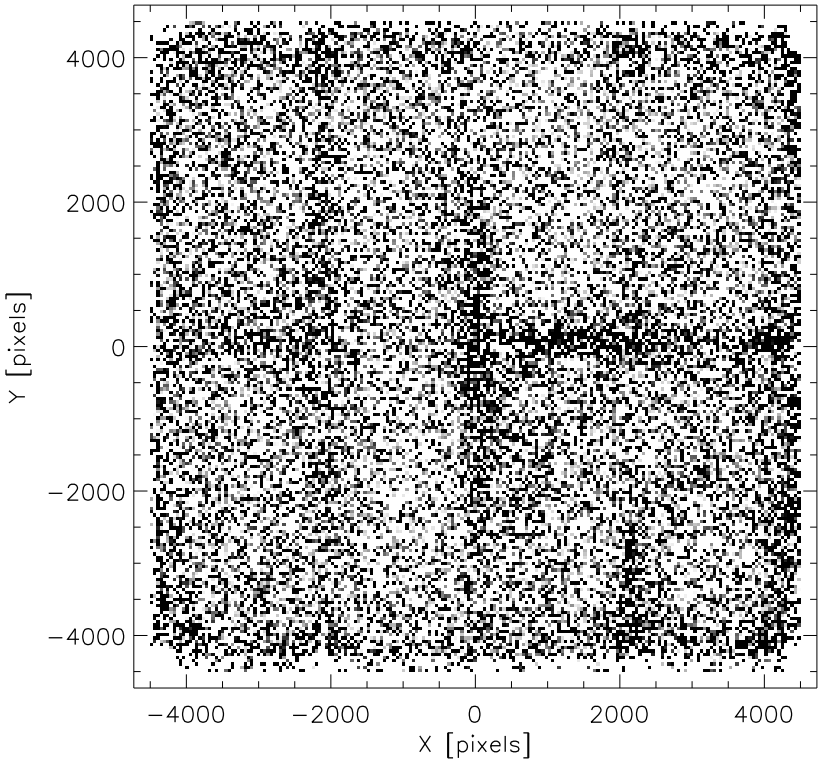

Figure 3.7: Residual absolute ellipticities of the stars after correction for the PSF, represented as a grey scale, dark where the residual signal is higher and lighter where the PSF correction is more efficient. The residuals are most prominent in regions of the image not covered by all individual exposures, where the PSF model is probably less accurate, resulting in the grid pattern around the eight chip-like regions as shown in Figure 3.5.

Other effects

As we show later, we attempt to separate the foreground from the background using a magnitude selection. Any faint foreground members contaminating our source sample will not carry a lensing signal, diluting the final detection. Another possible source of error may come from faint group members, not identified as such spectroscopically, that contaminate our sample of background sources. This is a possibility, as the survey specifically targets areas on the sky with an overdensity at the lensing redshift. If this affects our signal, we expect it to be diluted as well (Mandelbaum et al. 2006).

In the next section, where we determine the foreground-background separation and calculate lens signal and efficiency, we will show that this contamination is likely to be minimal.

3.4.3 Background redshift distribution

Since the groups are relatively close by, the lensing geometry is far from optimal. However, an advantage is that we can use many background sources, selecting all sources with $I_{AB} \geq 19$,

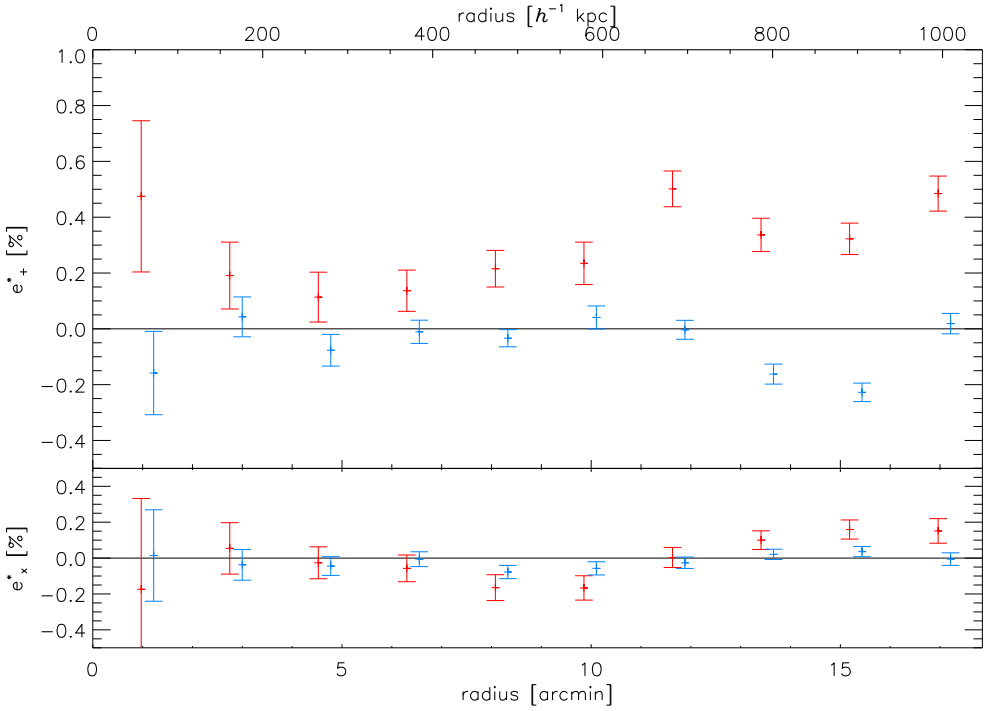

Figure 3.8: The tangential ellipticity (e_+) and cross signal ($e_\times$) carried in stars that are present in all individual exposures, before (red) and after (blue, slightly offset to the right) correction for the PSF. The total number of stars used is $\sim 3.5 \times 10^4$.

resulting in a selection of $19 \leq I_{AB} \leq 23$. Using the first epoch results of the VIMOS VLT Deep Survey (Le Fèvre et al. 2005, hereafter VVDS), we estimate a median redshift of the selected background sources of $z \sim 0.43$.

In Figure 3.9 we show the expected redshift distribution of the selected source sample, taking into account the full VVDS redshift distribution for each magnitude and the individual weights described in Section 3. The dashed line represents the median redshift of the ZENS group sample.

The strength of the gravitational shear signal for a given lens depends of the distances of the observer to the lens (D_d), the background sources (D_s) and the distance from the lens to the source (D_{ds}). With lens redshifts between $0.05 < z < 0.0585$, we calculate an angular diameter distance range of the lenses to be $202 \leq D_d \leq 233\ h^{-1}$ Mpc. Taking into account the variation in lens redshifts and the full estimated background redshift distribution, we calculate the variation in lensing efficiency D_{ds}/D_s, shown in Figure 3.10.

The weighted mean lensing efficiency is found to be $D_{ds}/D_s = 0.86$, shown as the dashed line in Figure 3.10, offset from the main peak due to the skewdness of the distribution. Since the gravitational shear signal is linear in D_{ds}/D_s, we can use this single number to relate reduced shear to physical quantities such as velocity dispersion and lensing mass.

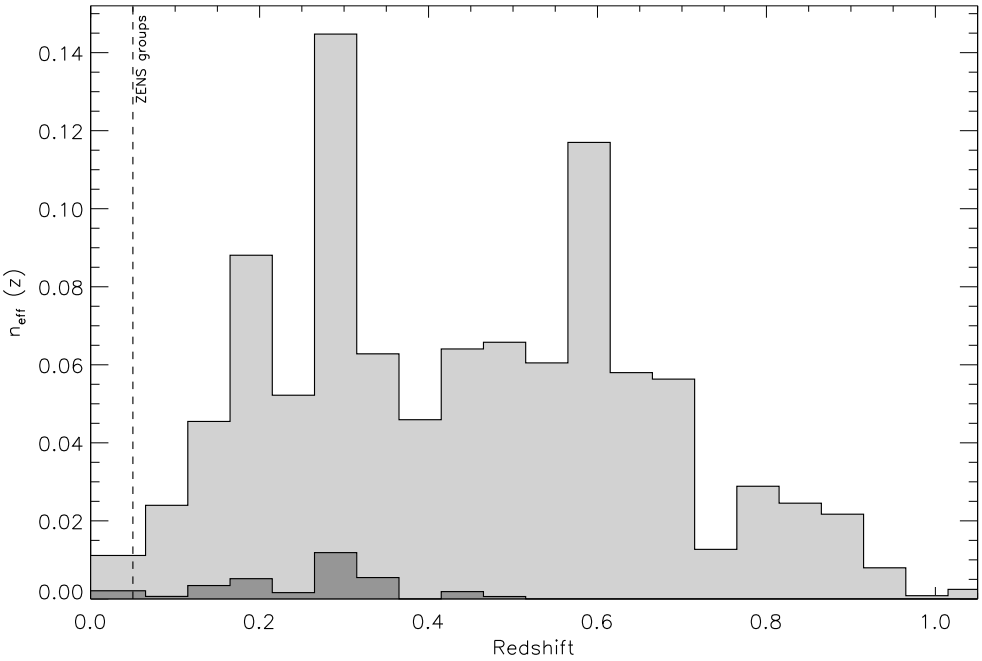

Figure 3.9: Expected redshift distributions for selected background sources with $I \geq 19$, represented as part of the effective total source selection. The high redshift tail of the distribution extends beyond the plot. The dashed line shows the median ZENS group redshift. For completeness, the dark grey histogram shows the expected redshift distribution of sources with $18 \leq I \leq 19$, corresponding to Figure 3.2.

Foreground-background separation

Comparing to the VVDS redshift distribution, we expect about $\sim 0.6\%$ of our background sources to be at the same or lower redshift than the groups. More strictly, sources at or just beyond the lens redshift can be seen as contamination as well as they will not carry much signal and mostly contribute noise. As a more conservative estimate, we expect $\sim 3.5\%$ of our background selection to lie at a redshift below $z = 0.1$. For foreground objects unrelated to the galaxy groups, this should be a fair indication. However, as said before, the ZENS targets areas on the sky with an overdensity at the lensing redshift, so these estimates should be read as lower limits due to possible faint group members that haven't been spectroscopically identified in the 2PIGG catalogue.

If there is a significant contamination of unidentified, faint group members, we expect an increased source density near the center of the groups, instead of a uniform background distribution. We attempt a more accurate estimate of the possible contamination by randomizing positions of background sources before only selecting sources that fall on the chip-like areas as described in Section 4. We use 1000 realizations for each of the fields and mask the areas where one or more of the individual exposures has a gap between the chips. We then count the sources in bins around the group centers and compare this to the actual source count in Figure 3.11.

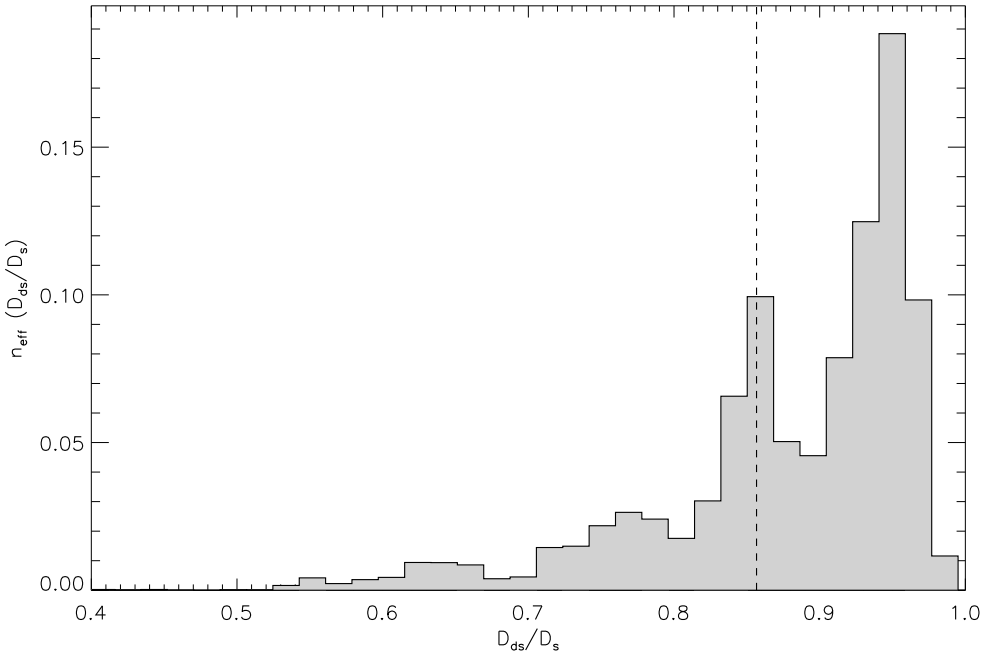

Figure 3.10: Expected lensing efficiency D_{ds}/D_s distribution for selected background sources with $I \geq 19$, represented as part of the effective total source selection. The dashed line shows the weighted mean lensing efficiency.

We normalize the average source count of the 1000 realizations to 100% in each bin and normalize the source count of the actual detected sources accordingly. The shaded grey area represent the variation in the randomizations. The red line representing the normalized, actual source count shows slightly more deviation from the simulated source counts than is expected from statistical variation, but we do not see a clear increase in source density in the central bins.

This method allows us to take into account the variation in areas masked between fields, due to different dither patterns, as well as source density variations between fields and the expected locations of the group centers with respect to the center of the images. This does not account for more complex effects, such as spacial gaps in detection due to very bright stars (an example of which can be seen in the center of Figure 3.4) or extraction flags due to coinciding bad pixels from different exposures. It should therefore be kept in mind that Figure 3.11 serves as an indication.

3.5 Gravitational shear signal and mass estimates

Weighting each field according to the density of background sources and their associated weights, we derive from the 2PIGG catalogue an average velocity dispersion of $\sigma = 229 \pm 21$ km s^{-1} and derived dynamical mass (Eke et al. 2004) of this group sample of $M_\sigma \simeq 4.1 \pm 1.1 \times 10^{13} h^{-1} M_\odot$.

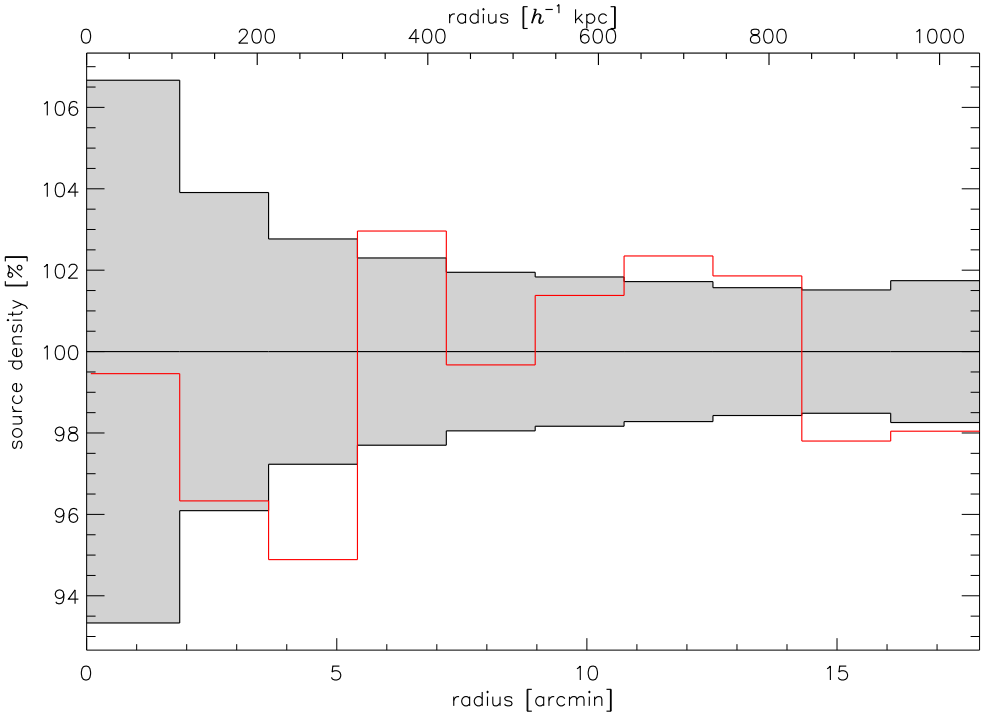

Figure 3.11: Source counts in bins around the group centres *(red line)*, compared to 1000 randomisations. The mean simulated source counts are normalised to 100% and the actual data counts are normalised accordingly. The shaded grey area represents the statistical variation in the randomisations.

This section will cover the estimation of the reduced shear signal, using a weighted statistical mean and convex hull peeling (CHP), to assess the influence of outliers. We estimate the signal around the luminosity-weighted mean (LWM) positions of the member galaxies and around the brightest group galaxies (BGGs). To relate our shear signal to physical quantities such as velocity dispersion an mass distribution, we fit a singular isothermal sphere (SIS) and a Navarro, Frenk & White (Navarro et al. 1996, NFW) profile to the ensemble average, and briefly touch upon how well the dynamical and luminous properties of the group correlate with the lensing signal.

3.5.1 Convex Hull Peeling

Mathematically, the convex hull of a set of points S in $\mathbb{R}^n$ is the intersection of all convex sets in $\mathbb{R}^n$ containing S. For our purposes, the convex hull of a two dimensional set of (g_1, g_2) points is the minimum subset of points that, if connected, forms a polygon that encloses the rest of the set.

The CHP or "onion peeling" method for determining the data center of a convex set, equivalent to the median for one dimension, consists of removing (peeling away) the convex hull and repeating the process for the remaining subset of points, until one point or no points are left. If one point is left, it determines the two dimensional median. If no points are left, the

mean of the last convex hull determines the two dimensional median, similar to the median in one dimension.

The main advantage of CHP is a lower sensitivity to outliers. Disadvantages include a less accurate determination of the underlying (g_1, g_2) (depending on the point cloud distribution) and the inability to apply weights to individual shear estimates. Here, we use it as an alternative to a direct weighted average, to asses the sensitivity to outliers of our shear determination.

3.5.2 Group centre of mass

One of the key problems in dealing with light galaxy groups is the determination of the center of mass. We discuss a priori the motivation for the two most likely tracers for the group center of mass, the LWM position and the BGGs.

Without external information, such as x-ray observations for heavy groups and clusters (e.g. Leauthaud et al. 2010), the only way to estimate the position of the center of mass of each group is using the luminous components, i.e. the member galaxies. One can either use the average position of the member galaxies, possibly weighted by their luminosities, or assume that the brightest member galaxy is also the heaviest and is on average located close the the center of the group halo. One can't use the lensing signal itself to estimate the position of the center of mass, not only because in this case the groups are too light to be detected in a projected mass reconstruction, but also because the signal would, by construction, be biased towards positive noise peaks.

For this group sample, the weighted and unweighted average positions correspond well with each other, and we decide to use the luminosity weighted mean positions. For groups with only a few members and a dominantly luminous galaxy, the LWM position and the position of the BGG lie close to each other, whereas the richer groups provide more statistical power.

In Figures 3.12 and 3.13 we plot in dark and light grey the predicted tangential shear signal around the LWM group positions and the BGGs, using for simplicity a SIS model based on the 2PIGG velocity dispersion and the background source positions and weights. To account for the complex masking we applied, we used the locations of the sources used for shear measurements in order to make an accurate prediction for this lens sample and data set. First we predict the signal around the LWM positions, both for the case where these would be a perfect tracer for the center of mass and if the BGGs would actually represent the center of mass. We then do the same for the expected signal around the BGGs in both cases. It is clear from Figures 3.12 and 3.13 that an accurate estimate for the center of mass is paramount.

Overplotted are the weighted mean tangential shear measured with the KK and TS pipelines in each bin. As in Figure 3.3, the two pipelines agree very well within error bars. In both plots, the cross signal is consistent with zero, as is required by theory. In the left plot, a clear positive signal can be seen around the LWM group positions, whereas in the right plot, the signal is consistent with zero on almost all scales around the BGGs. We also note the diminished signal in the outer bins and propose that this is caused by residual PSF distortion, similar to Figure 3.8.

This *suggests* that, at least for this group sample, the LWM positions represent the positions of the center of mass better than the BGGs. However, we should be cautious against

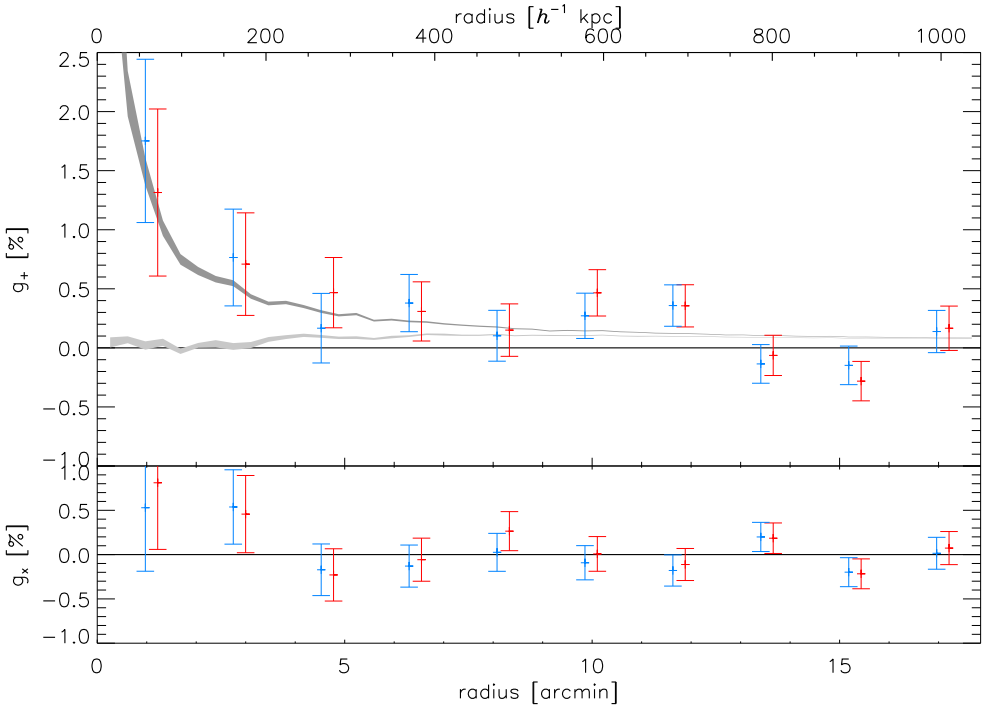

Figure 3.12: Binned tangential shear measured around the LWM group positions. The KK *(blue)* and TS *(red)* measurements agree well within error bars. The dark grey shaded area is the predicted tangential shear for the group velocity dispersions from the 2PIGG catalogue, assuming the centre of mass to coincide with the LWM group positions and assuming a SIS density profile for each group, where the thickness represents the spread due to the variation in σ within the group sample only. The light grey shaded area is the same around the BGGs.

deciding on the measurement that corresponds best to expectations and note that the measurement is very noisy. We have motivated our choice for two possible tracers for the underlying center of mass and we will continue our analysis using the signal around the LWM group positions, but we do not presume this assumption to be a general conclusion for light galaxy groups.

One should keep in mind that for a less accurate estimate of the group center of mass, the signal is more diluted. This means that a possible improvement in group center determination could increase the signal and our result might be slightly biased low. However, this effect could be well within error bars and the conclusion that our result is a lower limit is likely too strong.

We further note that all bins are completely independent in the sense that each background source is used only once, neglecting the $\sim$ 600 sources ($\sim$ 0.5%) detected in two fields. At larger radii, the effect of background large-scale structure (LSS) can give a correlation (Hoekstra 2003). Since the groups are at such a low redshift, this effect might be present, depending on the actual redshift of the lensed background sources.

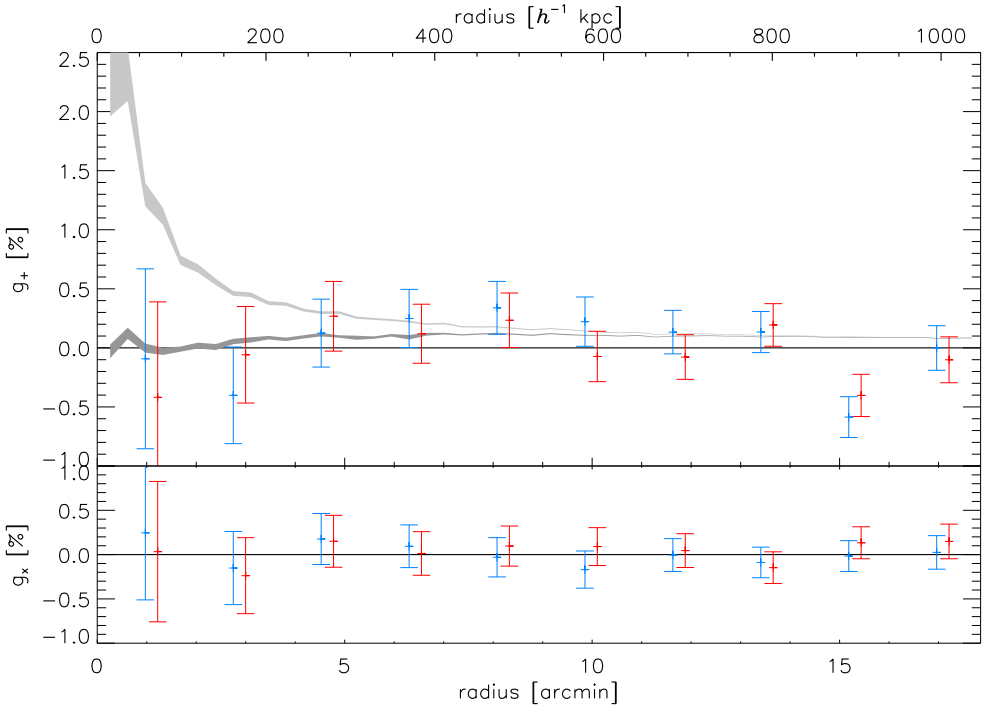

Figure 3.13: Binned tangential shear measured around the BGGs. The KK *(blue)* and TS *(red)* measurements agree well within error bars. The dark grey shaded area is the predicted tangential shear for the group velocity dispersions from the 2PIGG catalogue, assuming the centre of mass to coincide with the LWM group positions and assuming a SIS density profile for each group, where the thickness represents the spread due to the variation in σ within the group sample only. The light grey shaded area is the same around the BGGs.

3.5.3 Velocity dispersion

To compare our lensing signal directly to the dynamical velocity dispersion σ_{dyn}, we fit a SIS model. In Figure 3.14, we show the resulting fit to the KK and TS measured tangential shear, using a weighted mean and a CHP radial binning of the data. Based on Figure 3.8, we exclude the outer three bins from our fit, although we note that both in Figure 3.8 and Figure 3.14 the outermost bin agrees very well with prediction and fit.

We derive $\sigma_\gamma \simeq 283^{+94}_{-150}$ km s^{-1} for Shapelets and $\sigma_\gamma \simeq 286^{+99}_{-164}$ km s^{-1} for KSB+. If we use CHP to bin the KK data, we find $\sigma_\gamma \simeq 251^{+90}_{-151}$ km s^{-1}. In Table 3.1, we summarize the results of these fits.

The results agree very well with each other and with the dynamical estimate of $\sigma_{dyn} = 229 \pm 21$ km s^{-1}, although the error estimates show that this is a noisy, albeit significant, result.

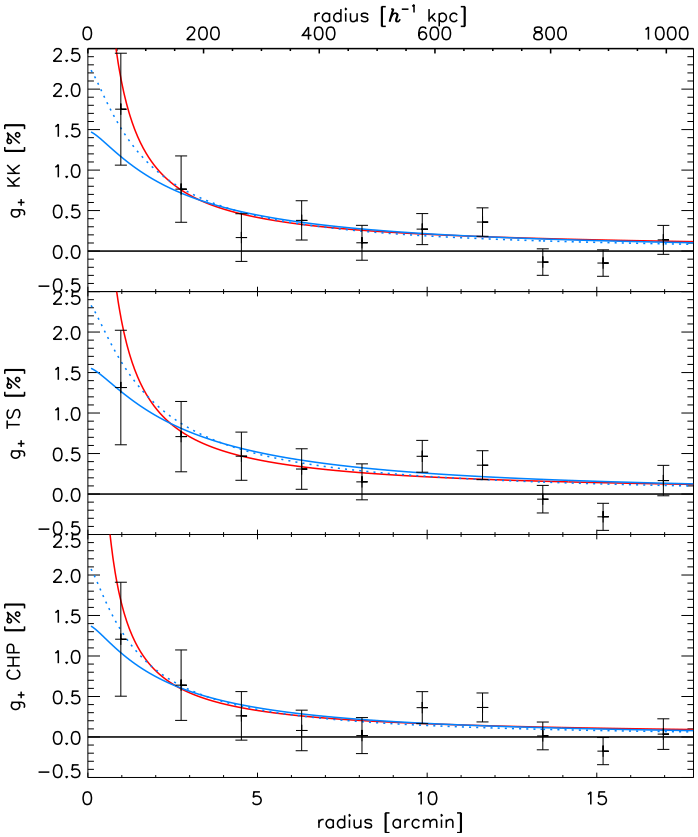

Figure 3.14: The best fit tangential shear profiles for the weighted averaged KK *(upper panel)*, the weighted averaged TS *(middle panel)*, and CHP KK *(lower panel)* bins. The red line is the best fit SIS profile and the blue lines are the best fit NFW profiles, assuming mass-concentration relations with $c_0 = 7$ *(solid)* and $c_0 = 10$ *(dotted)*.

3.5.4 Mass and concentration

We attempt to derive an estimate for the mass and concentration of the average group halo by fitting a NFW profile, where we keep M_{200} and c as free parameters. In Figure 3.15, we show the χ^2 distributions over the parameter space, we we have again excluded the three outermost bins from the fit. We also summarize the results in Table 3.1.

While M_{200} is relatively well determined, it is difficult with the low signal-to-noise of our result to get constraints on the concentration parameter c. Only for the weighted KK bins a lower limit on c can be determined.

Various studies have indicated that the halo mass and concentration are actually correlated, both simulations (see e.g. Neto et al. 2007, Duffy et al. 2008) and observations (Mandelbaum et al. 2008, M08). Following M08, we assume a mass-concentration relation of the

Method	Full group sample				
	SIS	NFW			
		Full fit		$c_0 = 10$	$c_0 = 7$
	σ_γ	M_{200}	c	M_{200}	M_{200}
KK	283^{+94}_{-150}	$2.0^{+3.3}_{-1.4}$	$6.8^{+5.8}_{-4.0}$	$2.3^{+2.5}_{-1.6}$	$2.8^{+3.6}_{-2.1}$
TS	286^{+99}_{-164}	$3.2^{+4.3}_{-2.4}$	$3.1^{+4.5}_{-3.1}$ (1)	$2.7^{+3.0}_{-2.0}$	$3.5^{+3.9}_{-2.5}$
CHP	251^{+90}_{-151}	$1.9^{+2.4}_{-1.2}$	$2.0^{+6.5}_{-2.0}$ (1)	$1.6^{+1.9}_{-1.2}$	$2.0^{+2.6}_{-1.6}$

Table 3.1: The best fit profile values for the weighted mean KK and TS measured shear and CPH bins for comparison, for the full group sample. Velocity dispersion σ_γ in [km s^{-1}] and masses M_{200} in $[10^{13}h^{-1}M_\odot]$. From left to right: the best fit SIS velocity dispersion; the best NFW fit for two independent parameters; M_{200} for $c_0 = 10$ and $c_0 = 7$.
(1) Lower limits not constrained.

form

$$c = \frac{c_0}{1+z}\left(\frac{M}{M_0}\right)^{-\beta} \tag{3.8}$$

where we assume $\beta = 0.1$, $M_0 = 10^{14}h^{-1}M_\odot$.

Figure 3.15 shows this relation for $c_0 = 7$, 10, and 13. Our sample of light galaxy groups falls right in the gap in mass range in M08, between L_* lenses and richer galaxy groups. Given the low lensing signal of our data, we only fit the resulting one parameter profile for $c_0 = 7$ and 10 and present the results in Table 3.1. Figure 3.14 shows the corresponding best fit NFW profile for a fixed mass-concentration relation with $c_0 = 7$ and $c_0 = 10$.

3.5.5 The heaviest groups

Since most of our groups have only a few members, with more than 75% having $N \leq 10$, an important question is which observed group property (taken from the 2PIGG catalogue directly) is a good indicator for the total group mass. Since gravitational lensing is sensitive to all gravitational matter, luminous and dark, it is instructive to compare to group properties based on the luminous content only.

To investigate how the lensing signal as a tracer of the total (projected) mass distribution correlate with various possible tracers for group mass from the 2PIGG catalogue, we split our group sample by dynamical velocity dispersion σ_{dyn}, total group luminosity L and group richness N. For simplicity we again assume a mass-concentration relation with $c_0 = 7$ for the NFW profile in all cases.

Table 3.2 presents the results for each pipeline and binning method for the various selections. Although there is an overall increase in significance for the estimate of σ_γ, there is no observable trend over selection method, pipeline or binning method. For the M_{200} estimate, the selection seems to have no consistent effect.

It is clear that for this study, we are limited by the signal-to-noise of the lensing signal. These considerations are important, however, when comparing studies of galaxy groups based

Method	Heaviest groups					
	Selection					
	σ_{dyn}		L		N	
	σ_γ	M_{200}	σ_γ	M_{200}	σ_γ	M_{200}
KK	356^{+102}_{-145}	$3.6^{+5.7}_{-3.0}$	333^{+105}_{-161}	$3.5^{+5.5}_{-2.9}$	294^{+101}_{-164}	$2.9^{+4.4}_{-2.4}$
TS	329^{+102}_{-152}	$3.0^{+4.7}_{-2.5}$	274^{+100}_{-172}	$2.1^{+2.9}_{-1.7}$	263^{+94}_{-157}	$2.4^{+3.2}_{-2.0}$
CHP	251^{+98}_{-187}	$2.5^{+3.6}_{-2.1}$	276^{+101}_{-178}	$2.4^{+3.7}_{-2.0}$	297^{+99}_{-157}	$3.2^{+4.5}_{-2.6}$

Table 3.2: The best fit profile values for the weighted mean KK and TS measured shear and CPH bins for comparison, for the 'heaviest' groups. Velocity dispersions σ_γ in [km s^{-1}] and masses M_{200} in $[10^{13}h^{-1}M_\odot]$, with $c_0 = 7$ assumed in all cases. From left to right: σ_γ and M_{200} for groups with the highest dynamical σ_{dyn}; total luminosity L; richness N .

on and using different methods, such as lensing, dynamics and, for heavier groups, X-ray observations.

3.6 Conclusions

We have been able to determine the gravitational shear signal around a sample of nearby light galaxy groups, making use of extended sky coverage, providing us with more than 10^5 background sources, and careful indentification of possible sources of systematic errors.

3.6.1 Shape measurements

A good understanding of possible systematic effects is paramount for an accurate determination of a subtle signal.

We have used two independent shape measurement methods, the Shapelets pipeline of Kuijken (2006) and the TS implementation of KSB+ described in Erben et al. (2001), both tested in STEP. Both methods yield very consistent results and using the shapelet pipeline we also find consistency between different single exposures and in overlapping fields. This leads us to conclude that the shape measurements are robust and reliable.

Our observations are well covered by foreground stars, with on average $N_* \approx 900$ per field for a well sampled PSF. We have used the residual differences between the actual stellar shapes and the PSF model as a diagnostic that should not be affected by the specific properties of this data set. We have shown that, except for the regions in the image stacks that are not covered by one or more individual exposures, the PSF model seems to be very accurate, leading to residual stellar distortions that are consistent with zero in both ellipticity components on almost all scales. We therefore conclude that a single, overall PSF model is not accurate in these regions with partial coverage and exclude for our analyses both stars and sources from these areas. We do caution for a residual tangential PSF distortion on large scales at the $\sim 0.1\%$ level in the stars and based on these tests do not include those scales in the final lensing analyses.

Using SDSS coverage of $\sim 30\%$ of our observations to test for any astrometric distortion effect, we found excellent agreement, with uncertainties at the $\sim 0.01\%$ level in order of magnitude. Using the VVDS magnitude-redshift observations, we estimate our foreground-background separation to be accurate, expecting less than 1% contamination of faint foreground sources. To account for the image geometry and complex masking pattern, we have used 1000 randomisations of background positions to look for any trend that could indicate contamination of our source sample by unidentified faint group members and found none. We are confident that any of these effects are negligible compared to the intrinsic variance for this data set.

3.6.2 Measured signal

Using both the LWM group positions and the BGGs as tracers for the underlying centre of mass, we find a significant tangential signal around the LWM positions. The absence of a signal around the BGGs underlines the sensitivity of the signal to the accuracy in the determination of the center of mass.

Analysing the signal around the LWM group centres, we use both a statistical mean and a CHP binning scheme, as the former is an unbiased estimator while the latter is less sensitive to outliers. Well within error bars, we find good agreement between shape measurement pipelines and between binning methods, showing the robustness of the detected signal.

3.6.3 Profile shapes

We have fitted both a SIS and a NFW profile to our measured signal and derived estimates for the velocity dispersion σ_γ, halo mass M_{200} and concentration c, summarised in Tables 3.1 and 3.2, that agree well with dynamical estimates (Eke et al. 2004) and studies of light galaxy groups at higher redshift (Parker et al. 2005). Although the unfavourable lensing geometry, range in group size and low average group mass leads to large error bars, the estimations for σ_γ and M_{200} are significant. We conclude that it is not possible to accurately constrain c as a free parameter with this data set.

We also assumed a mass-concentration relation and looked at plausible values for the normalisation constant c_0 based on M08. A value of $c_0 = 7$ seems to agree best with results from both pipelines and binning methods. Using this value, we have investigated the correlation of our lensing signal with group properties that possibly trace the halo mass, velocity dispersion σ_{dyn}, luminosity L, and richness N. Although there seems to be an increase in lensing signal overall, the increase in uncertainties from using half of our data set limits the significance of this trend.

3.6.4 General conclusion

Using independent shape measurement methods, we find overall a good agreement between gravitational lensing and dynamical methods on the different estimations of the average group mass content. Our lensing results, although having a low signal-to-noise ratio, agree well with those obtained from groups at higher redshift. Furthermore, we have shown that weak gravitational lensing works for these low redshift lenses, where the weak signal barely extends

above the intrinsic shape noise of our sample of background galaxies, filling in gaps in mass and redshift ranges.

3.6.5 Future work

Our weak lensing study can be an important, independent result complementing other studies of the group environment (see Carollo et al. 2009, *in prep.*), which is the most common galaxy environment and perhaps dominant in galaxy evolution (see e.g. Tran et al. 2009). Given the current sample, the lightness of the groups and the lensing geometry, we expect to have reached the limits of what can be obtained with our current data. Our results show that lensing can be an useful, practical technique to study matter distributions down to low redshift and low density.

We look forward to robust catalogues of galaxy groups becoming available for large scale surveys better or specifically suited for lensing, such as the CFHTLS (see e.g. Parker et al. 2007) or the soon to commence KIDS, which will cover an important part of this group sample. More detailed studies will be possible with these big surveys, allowing one to investigate trends e.g. with group richness, redshift and proximity to LSS. Given the promising results so far in this field, the study of galaxy groups using gravitational lensing has much potential left to be explored.

Acknowledgements

We like to thank Malin Velander for making her NFW fitting routines available to us. The CHP method was first brought to our attention by a poster presentation of Hyunsook Lee at Penn State University. MS acknowledges support from the Netherlands Organization for Scientific Research (NWO). TS acknowledges support from the Netherlands Organization for Scientific Research (NWO), NSF through grant AST-0444059-001, and the Smithsonian Astrophysics Observatory through grant GO0-11147A.

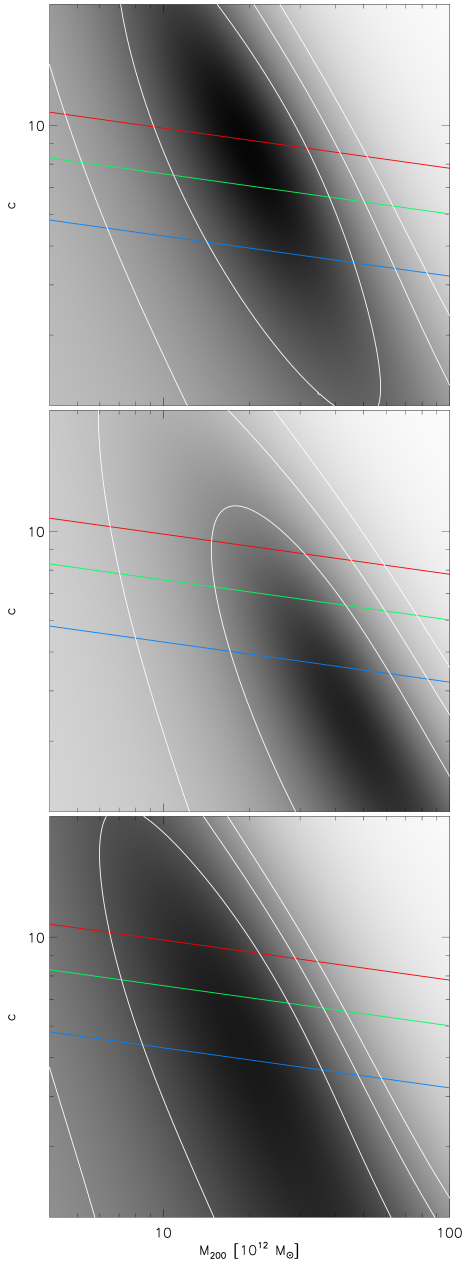

Figure 3.15: The χ^2 distributions *(greyscale)* for the M_{200}, c fits to the weighted averaged KK *(upper panel)*, the weighted averaged TS *(middle panel)*, and CHP KK *(lower panel)* bins. The white contours show the 68%, 95%, and 99% confidence limits. The red, green and blue lines represent mass-concentration relations assuming c_0 = 13, 10, and 7 respectively.